Applied Surface Science 416 (2017) 605–617

Contents lists available at ScienceDirect

Applied Surface Science

journal homepage: www.elsevier.com/locate/apsusc

Mechanical, structural and dissolution properties of heat treated thin-film phosphate based glasses

Bryan W. Stuart, Miquel Gimeno-Fabra, Joel Segal, Ifty Ahmed, David M. Grant*

Advanced Materials Research Group, Faculty of Engineering, University of Nottingham, UK

ARTICLE INFO

Article history:
Received 12 December 2016
Received in revised form 6 April 2017
Accepted 15 April 2017
Available online 18 April 2017

Keywords:
Heat treatment
Phosphate glass
Mechanical properties
Ion leaching
Osseointegration
Thin films

ABSTRACT

Here we show the deposition of 2.7 μm thick phosphate based glass films produced by magnetron sputtering, followed by post heat treatments at 500 °C. Variations in degradation properties pre and post heat treatment were attributed to the formation of Hematite crystals within a glass matrix, iron oxidation and the depletion of hydrophilic P-O-P bonds within the surface layer. As deposited and heat treated coatings showed interfacial tensile adhesion in excess of 73.6 MPa; which surpassed ISO and FDA requirements for HA coatings. Scratch testing of coatings on polished substrates revealed brittle failure mechanisms, amplified due to heat treatment and interfacial failure occurring from 2.3 to 5.0 N. Coatings that were deposited onto sandblasted substrates to mimic commercial implant surfaces, did not suffer from tensile cracking or trackside delamination showing substantial interfacial improvements to between 8.6 and 11.3 N. An exponential dissolution rate was observed from 0 to 2 h for as deposited coatings, which was eliminated via heat treatment. From 2 to 24 h ion release rates ordered P > Na > Mg > Ca > Fe whilst all coatings exhibited linear degradation rates, which reduced by factors of 2.4–3.0 following heat treatments.

1. Introduction

Hydroxyapatite (HA) emerged as an osteoconductive coating in the 1980s and remains an industrial surface treatment for orthopaedic integration [1]. Second generation bioceramics facilitated interfacial bonding between the host tissue and implant [2]. Plasma sprayed HA is a ceramic coating layer with a Ca/P ratio of 1.67, similar in composition to the cortical bone. Bone like layers on metallic hip stems or dental screws promote adhesion of osteoblast cells and protein attachment for bone regeneration and osseointegration [3–5].

Plasma sprayed HA layers have been known to delaminate entirely at the interface, preventing complete osseointegration via the coating layer or causing integration directly with the implant surface. A study by Bloebaum et al. found particles of HA up to 75 μm, and metallic particles due to wear of the underlying implant embedded in the acetabular cup [6]. Despite improvements, aseptic loosening remains the biggest cause of implant failure, responsible for ≈40% of revisions [7].

The key factor for bioactivity is the stimulation of osteoblasts for collagen secretion and subsequent mineralisation of bone, assisted by creating an environment for osteoconduction at the surface of the implant device [8]. Collagen protein fibrils are laid down by osteoblast cells along the bone surface, facilitating regeneration from the creation of a extracellular matrix (ECM) [3]. Ca and P within the formed net of the ECM may mineralise to form crystallised bone in the form of HA. Phosphate Based Glasses (PBG) represent a third generation biomaterial which is fully resorbable in aqueous media and could repair the surrounding tissue by activating a controlled cellular response through the delivery of potentially therapeutic ions [1]. Research on PBGs has included Mg [9], Ca [10,11], Sr [12,13], F [14], which have been used for bone tissue generation, Ti [15–17], Fe [18,19] to improve durability, Cu [20] and Ag [21,22] for their antibacterial properties.

Pre-existing thermal technologies have been used to produce silicate based glass (SBG) coatings with mixed success. The inherent temperatures associated with the thermal processes, make the production of either adherent or amorphous glasses impractical without delamination, cracking or crystallisation. The thermal expansion mismatch leads to interfacial stresses and poor adhesion [23,24]. For example, Bioglass® 45S5 was plasma sprayed with failure occurring from thermally induced residual stresses at the Ti coating interface [25]. Bolelli et al. utilised suspension high velocity flame spraying [26] whilst Gomez-Vega et al. formed 25–150 μm thick coatings via an enamelling process [24].

* Corresponding author.
E-mail address: david.grant@nottingham.ac.uk (D.M. Grant).

http://dx.doi.org/10.1016/j.apsusc.2017.04.110

Thin coatings in particular may be desired to prevent brittle failures associated with shear during implantation. A comprehensive review by Mohseni et al. concluded that magnetron sputtering produced the greatest interfacial adhesion of HA on Ti6Al4V after investigating 9 deposition methods including plasma spraying, hot isostatic pressing, thermal spray coating, dip coating, pulsed laser deposition, electrophoretic deposition, sol gel, ion beam assisted deposition and PVD sputtering [27].

RF magnetron sputtering of SBG was explored by Mardare et al. [28] and by Stan et al. [29]. The manufacturing complications associated with PBG coatings during sputtering has been demonstrated elsewhere [30], whilst a previous publication showed structural variability between compositionally equivalent melt quenched and PVD coatings, showing greater bulk and surface polymerisation in coating compositions [31].

The melt quenched PBG composition P_2O_5-40 MgO-24 CaO-16 Na_2O-16 Fe_2O_3-4 mol% (denoted MQ: P40) has been extensively researched for the production of degradable glass fibres [32]. Hassan et al. demonstrated good cytocompatibility with MG63 osteoblast cells, indicating comparable results to the tissue culture plastic control samples [33]. Therefore the work presented here investigates the sputtered coating composition; P_2O_5-40 MgO-24 CaO-16 Na_2O-16 Fe_2O_3-4 mol% applied to Ti6Al4V, specifically exploring the effects of surface topography and post deposition annealing on structural, mechanical, degradation and ion release properties.

2. Methodology

2.1. Target preparation T1: P51.5 Fe5 and melt quenched: P40

Pre-calculated (mol%) proportions of precursor salts namely sodium dihydrogen phosphate (NaH_2PO_4), calcium hydrogen phosphate ($CaHPO_4$), magnesium phosphate dibasic trihydrate ($MgHPO_4{\cdot}3H_2O$), iron phosphate dehydrate ($FePO_4{\cdot}2H_2O$) and phosphorous pentoxide (P_2O_5) (Sigma Aldrich, U.K.), were thoroughly mixed then preheated at 400 °C to dehydrate. The mixture was then melted in a Pt:Rh (90/10 wt%) crucible at 1200 °C for 2 h in air. The targets were formed by quenching the molten mixture at 450 °C followed by slow cooling to room temperature. The target mould and the subsequent target measured 75 ± 2 mm in diameter and 6 ± 1 mm in thickness. See Table 1 for target composition. MQ: P40 was similarly cast into 9 mm diameter rods and cut into 7 mm cylinders using a diamond saw.

2.2. RF magnetron sputtering

The coatings were deposited via a custom in-house designed Physical Vapour Deposition (PVD) rig using RF (13.56 MHz) magnetron sputtering, with a PBG target (denoted T1: P51.5). The chamber was pumped down to a vacuum using a combination of a rotary (Edwards E2M-18) and turbo molecular pump (Edwards EXT250) to a base pressure $<7 \times 10^{-3}$ Pa. Phosphate glass deposition was performed at 60 ± 1 W power (13.6 kW m^{-2}) for 1165 min to a coating thickness of 2.67 ± 0.09 μm at a pressure of 10 ± 0.05 mTorr of 99.99% pure-shield argon. The distance between target and substrate was also held constant at 4 ± 0.5 cm. Prior to deposition, targets were sputter cleaned for 30 min at 30 W and increased to 60 W for a further 30 min. The target glass has been labelled (T1), melt quenched glass rods as (MQ) and coatings as (C). Nominal compositions have been denoted by (N) whilst as prepared compositions assessed via EDX compositional analysis have been denoted by (AP). See compositions in Table 1.

2.3. Post deposition annealing

PBG coatings C2: P40HT30 and C3: P40HT120 were deposited as amorphous and subsequently heat treated in a Lenton tube furnace, with 99.99% pureshield argon to 500 °C at 10 °C min^{-1}. Coatings C2: P40HT30 and C3: P40HT120 were held for dwell times of 30 min and 120 min respectively. All samples were left to cool naturally to room temperature.

2.4. Thermo mechanical analysis

Thermal Expansion coefficient (TEC) was measured using Thermo Mechanical Analysis (TMA) via a TMA Q400. 50 mm long, 9 mm diameter MQ: P40 glass rods were heated up to 400 °C at a rate of 10 °C min^{-1}. The TEC measurements were obtained from a best-fit line between 50 and 300 °C. All expansion measurements represent the Standard Error Mean of $n = 3$ samples.

2.5. X-ray diffraction

Samples of the glass targets were ground to a fine powder for X-Ray diffraction (XRD) analysis (Bruker D8, Cu Kα source: λ = 1.5418 Å, 40 kV, 40 mA) conducted over a 2θ range from 15° to 65° with a step size of 0.04° in 2θ, and a dwell time of 5 s. In addition glancing angle XRD was performed on the deposited coatings utilising a step size of 0.02° in 2θ.

2.6. Energy dispersive X-ray spectroscopy

The compositions of the sputtering targets and sputtered coatings were determined via a Phillips XL30 SEM-EDX. Energy Dispersive X-Ray Spectroscopy (EDX) was conducted at a working distance of 10 mm at a minimum of 200,000 counts and a beam voltage of 15 kV. The electron beam current was optimised by increasing the spot size to obtain a minimum acquisition rate of 4000 counts s^{-1} whilst maintaining an acquisition dead time <30%.

2.7. Scanning electron microscopy

The coating cross sections and surface images were obtained via Scanning Electron Microscopy (SEM) using a Phillips XL30-ESEM. The working distance was kept constant at 10 mm, with a beam voltage of 15 kV. The precision of the EDX system was analysed over a repeated spot ($n = 5$), whilst coating homogeneity was assessed over ($n = 12$) random sample areas. Additionally, batch-to-batch variation ($n = 4$) was calculated and the estimated error is presented in Table 1.

2.8. Fourier transform infrared spectroscopy attenuated total reflectance

A Bruker Tensor Fourier Transform Infrared Spectrometer (FTIR) with an Attenuated Total Reflectance (ATR) attachment was used for all Infrared absorption measurements. A spectral resolution of 4 cm^{-1} over the wavenumber range 500–4000 cm^{-1} was set. All spectra obtained represent the average of 64 scans over the sample area.

2.9. Focussed ion beam scanning electron microscope

The coatings on Ti6Al4V substrates were sectioned and polished via a Focussed Ion Beam (FIB) using a Zeiss NVision 40 with a gallium milling source. The working distance was kept constant at 5 mm using a beam voltage of 5.00 kV. All sections were cut at a tilt angle of 54°.

Table 1
As prepared target, melt quenched and coating compositions mol%. Nominal composition (N) and as prepared (AP) were analysed by EDX.

Glass code nominal (N) vs. as prepared (AP)	P_2O_5	MgO	CaO	Na_2O	Fe_2O_3
	mol%				
T1: P51.5 (N)	51.50	18.50	14.00	11.00	5.00
T1: P51.5 (AP)	49.81 ± 0.11	19.31 ± 0.08	13.31 ± 0.09	13.15 ± 0.11	4.42 ± 0.53
MQ: C1: C2: C3: P40 (N)	40.00	24.00	16.00	16.00	4.00
MQ: P40 (AP)	39.64 ± 0.08	24.49 ± 0.08	15.59 ± 0.07	16.73 ± 0.06	3.55 ± 0.06
C1: P40AD (AP)	40.23 ± 0.19	23.83 ± 0.15	15.37 ± 0.15	16.75 ± 0.14	3.82 ± 0.53
C2: P40HT30 (AP)	40.71 ± 0.17	22.30 ± 0.13	16.59 ± 0.14	15.95 ± 0.15	4.45 ± 0.53
C2: P40HT120 (AP)	41.47 ± 0.37	22.58 ± 0.21	15.89 ± 0.16	15.93 ± 0.31	4.13 ± 0.53

2.10. X-ray photoelectron spectroscopy

X-Ray Photoelectron Spectroscopy (XPS) was conducted using a VG Scientific EscaLab Mark II with an Al kα non-monocromatic X-Ray source incident to the sample surface at ≈30°. Scans were collected at 20 mA and 12 kV emissions. The survey and high resolution spectra were scanned 3 and 5 times respectively, utilising step sizes of 1.0 and 0.2 eV for dwell times of 0.2 and 0.4 s respectively. Analysis and peak fitting was conducted using Casa XPS. All spectra were charged corrected for the C 1s emission to 284.8 eV. For compositional quantification, the area under the peak of the most intense photoelectron emission for each element was calculated and normalised to the overall area, utilising their Relative Sensitivity Factors acquired from the Scofield RSF library. For the high resolution spectra, relative peak positioning and peak areas due to spin orbit splitting were constrained based on the relationship of the electron subshell.

2.11. Atomic force microscopy

Atomic Force Microscopy (AFM) micrographs and roughness measurements were acquired in tapping mode via a Bruker Dimension Icon. AFM tips; model TAP525A 0.01–0.025 Ohm-cm Antinomy (n) doped Si were used. All measurements were acquired over a scan area of $20.0 \times 20.0 \mu m^2$. AFM analysis software Gwyddion was used for analysis.

2.12. Sample preparation for coating deposition

Substrates for coating were 1.5 mm thick, 10 mm diameter Ti6Al4V (grade 5) discs wire eroded from sheet. The discs were wet polished to a 6 μm finish using silicon carbide paper from grades P200-P4000 and further polished on a 0.25 μm chemomet finishing pad with the application of colloidal silica. The polished and sandblasted substrate roughness's were measured as 7 ± 1 nm and 696 ± 57 nm respectively ($n = 9$) via AFM. Samples were then ultrasonically cleaned for 10 min in acetone, followed by distilled water. 100 μm thick borosilicate cover slides were also coated to measure the coating thicknesses achieved. Prior to coating, the slides were platinum coated for 90 s at 1.2 keV in a Polaron sputter coater to enhance the interfacial contrast between coating and glass for microscopy analysis.

2.13. Degradation of coatings and ion release

The PBG coatings were deposited onto both polished and sandblasted Ti6Al4V (Grade 5) substrates by RF magnetron sputtering.

For SEM analysis the coated discs were submerged in 15 mL of distilled water (dH_2O) and incubated at 37 ± 2 °C. Isolated coated samples were observed at 16 h. The pH was measured pre and post degradation to ensure the solution did not become saturated. Samples could not be re-submerged following conductive coating for imaging due to contamination inhibiting degradation.

Mass loss per unit projected surface area was recorded for coatings on sandblasted substrates, as bulk coating lift off or delamination had been observed on polished C1: P40AD. Measurements were collected using a Mettler Toledo precision scale accurate to 0.01 mg. All samples were weighed prior to deposition and post deposition to determine the mass of the coatings. Samples were subsequently submerged in 15 mL of solution and incubated at 37 ± 2 °C ($n = 3$). At each time point the discs were removed, and placed in an oven at 50 °C for 1 h to remove surface moisture, prior to mass loss measurements. The solution was changed after 1 and 3 days.

To assess ion release, isolated samples ($n = 3$) for time points of 2, 16, 24 and 48 h were submerged in 15 ml of ultrapure Milli-Q water. Multi-element analysis of solutions was undertaken by ICP-MS (Thermo-Fisher Scientific iCAP-Q) utilising internal and external calibration standards, whilst samples were processed using the Qtegra™ software (Thermo-Fisher Scientific).

2.14. Scratch adhesion testing

Scratch Adhesion testing was conducted in accordance with the BS EN 1071-3:2005 standard, using a Bruker scratch tester and a Rockwell C Indenter. Progressive loads were applied over a distance of 3 mm with a pre load of 0.5 N followed by progressive loading to 30 N over a period of 180 s. All values represent the average of $n = 8$ scratches. The critical loads (L_c) were defined as the initial appearance of the failure mechanism along the scratch path or trackside.

2.15. Pull off adhesion testing

The pull off test was conducted in accordance with ASTM-D4541-09 using a precision adhesion testing apparatus (PAT Handy) manufactured by DFD instruments. Pull off stubs of 2.81 mm in diameter were used with a sample number of ($n = 8$). A thermally curing epoxy resin (DFD E1100S) was applied over the area of the stub and pressed onto the coating surface. The stub/substrates were placed on a heated plate at 140 °C for 60 min to cure.

3. Results

3.1. Composition and structural analysis

3.1.1. EDX

The coating composition P_2O_5-40 MgO-24 CaO-16 Na_2O-16 Fe_2O_3-4 mol% was investigated to observe the effect of heat treatment on the coating topography, crystallinity, degradation and mechanical properties. Elemental mol% compositions of MQ, C1, C2 and C3 were observed to vary by a maximum of 1.24, 1.53, 1.22, 0.82, 0.63 mol% for P_2O_5, MgO, CaO, Na_2O, Fe_2O_3, respectively. Variation may have been attributed to precision of the EDX

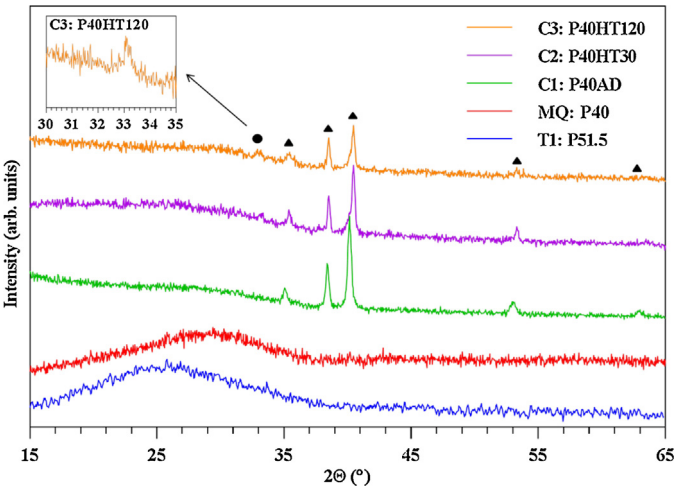

Fig. 1. XRD of C1: P40AD and C2: P40HT30 and C3:P40HT120 coatings. Substrate signal indicated (▲) titanium (ICDD PDF-00-001-1197). A crystalline phase corresponding to (●) Hematite (Fe_2O_3) (ICDD PDF-01-085-0599) emerged following C2: P40HT30 and C3: P40HT120. Amorphous humps were present in all samples from 15° to 40° (2θ). The deposition target T1: P51.5 was entirely amorphous.

method, consistency of the coating process and batch reproducibility [30,34].

3.1.2. XRD

Glancing angle XRD suggested an amorphous microstructure for C1: P40AD. Signal from the Ti substrate produced peaks associated with titanium ICDD PDF-00-001-1197. In addition a single diffraction peak emerged in C2: P40HT30 and C3: P40HT120 located at ≈33° (2θ) (see Fig. 1 Insert for magnified slow scan). This peak was attributed to the reflection (104) of Hematite (Fe_2O_3) (see Fig. 1). An amorphous diffraction hump remained present from 15° to 38° (2θ) following heat treatment. Structural and degradation properties of C1: P40AD and MQ: P40, have been previously published [30,35].

3.1.3. FTIR

IR absorption of the three coatings C1: P40AD, C2: P40HT30 and C3: P40HT120 contained peaks associated with vibrational modes located at ≈1280, 1200, 1100, 1055, 1012, 912, 769, 530 cm^{-1}. The position ranges and peak designations are detailed in Fig. 2. C1: P40AD showed weaker relative absorption at 1280 and 530 cm^{-1} attributed to Q^2 (PO_2) groups and Q^0 (PO_4^{3-}) respectively whilst C2: P40HT30 and C3: P40HT120 contained Q^2 (PO_2) shoulders at 1280 cm^{-1}. The band attributed to Q^0 (PO_4^{3-}) increased with intensity following C2: P40HT30 and C3: P40HT120 and may have been attributed to Hematite. According to Minitti et al. Hematite bands are located at 315, 461 and 560 cm^{-1}, overlapping the PO_4^{3-} band at 500–565 cm^{-1} [36,37].

The notable decline in the relative intensities of the peaks at 900, 769, and 530 cm^{-1} for all degraded samples may indicate possible cleavage of the P-O-P bonding, a reduction in Q^0 species or proportional increase in Hematite (Fe_2O_3) with respect to the amorphous phase (Fig. 2).

3.1.4. XPS

XPS survey spectra of C1, C2 and C3 showed the surface elemental compositions within the first 5–10 nm of the coating layer (Fig. 3A, C, E) [38]. Following heat treatment at the annealing temperature of 500 °C for both 30 min and 120 min, the peaks previously present in C1: P40AD for P 2p and P 2s at 132–140 eV and 185–195 eV (Fig. 3A) respectively were absent from the spectra of C2: P40HT30 (Fig. 3C) and C3: P40HT120 (Fig. 3E) showing a phosphorous deficiency in the surfaces of the heat treated coatings. Quantification of the composition in at% showed an increase in Fe content from 1.4% to 22.4% and 22.8% following HT30 and HT120 min (Table 2). The at% and mol% have been presented in Table 2.

The high resolution scan for Fe 2p for C1: P40AD could not be deconvoluted with a sufficient level of confidence based on low signal intensity and the presence of closely spaced binding energies attributed to the multiple chemical states (Fig. 3B, D and F). Gupta et al. showed over 20 peaks located between 708.3–713.6 eV which were attributed to FeO, Fe_2O_3, Fe_3O_4, FeOOH [39]. The peak positions were determined by analysis of standard reference materials. The asymmetrical peak shape towards 709.0 eV and the breath of the Fe 2p 3/2 spin orbital suggested the combined presence of Fe_2O_3, Fe_3O_4, and FeOOH [39]. Gupta et al. suggested peak 1 positions at 709.8 eV, 710.2 eV, 710.2 eV respectively with peak 4 positions at 712.3, 713.6 and 713.2 eV respectively [39].

Fe 2p showed improved resolution following heat treatment, with no apparent difference between C2: P40HT30 and C3: P40HT120. The satellite regions here were observed between 715.0–724.0 and 730.0–737.0 eV. Fe 2p has a spin orbit split (Fe 2p 1/2), generating spectral peaks located between 721.0 and 737.0 eV (Fig. 3D and F) [40,41]. The defined asymmetric peak positions of 710.4 and 710.6 eV, the narrowing of the Fe 2p 3/2 and 1/2 peaks and the satellite peak locations of 7.9/7.8 and 8.7/8.0 eV from the main spectral peaks for C2: P40HT30/C3: P40HT120 respectively (Fig. 3D and F) suggested the prominence of Fe_2O_3. Grosvenor et al. located satellite peaks for Hematite (α-Fe_2O_3), Magnetite (γ-Fe_2O_3), Lipidocrocite (γ-FeOOH), Magnetite (Fe_3O_4) to be spaced 8.3, 8.5, 8.0 and 5.9 eV from their electron spin orbital Fe 2p 3/2.

3.2. Adhesion and mechanical properties

3.2.1. Scratch testing

The mechanical properties of coatings C1: P40AD, C2: P40HT30 and C3: P40HT120 were determined by progressive scratch and tensile pull off testing (see Figs. 4–6). The scratch wear mechanisms have been labelled in accordance with the standard; BS EN 1071-3:2005 in order of critical load (L_cx) occurrence and were attributed to the initial indentation (scratch L_{c1}), (tensile cracking L_{c2}), (trackside delamination L_{c3}), (buckling and buckle spallation L_{c4}) and (Interfacial delamination L_{c5}) (Fig. 4A).

The trends showed a reduction in failure loads of all wear mechanisms following annealing for 30 min (Fig. 5A). The failure strengths appeared to recover following annealing for 120 min. A closer examination of the scratch results (C1: P40AD compared with C3: P40HT120) suggested that L_{c1} and L_{c2} occurred at higher loads, increasing from 1.0 to 2.5 N and 2.0 to 3.0 N respectively. The primary interfacial failure occurred by the mechanism of trackside delamination at 3.2, 1.5 and 3.0 N respectively for C1, C2, and C3. Notably; the increases in loading from initial scratch L_{c1} until the Interfacial delamination L_{c5} were 4.0, 1.3 and 2.0 N for C1, C2, and C3, whilst the failure loads of L_{c2}, L_{c3} and L_{c4} for coatings C2: P40HT30 and C3: P40H120 were closely spaced ranging from 0.1 and 0.3 N respectively (Fig. 5A). Scratch testing was additionally applied to coatings on sandblasted substrates as shown for C3: P40HT120 (Fig. 4). Observed failure mechanisms were limited to the initial scratch, buckle spallation and interfacial delamination. No coating fragmentation due to delamination along the trackside was observed (Fig. 4D). Coatings exhibited improved interfacial properties following substrate roughening via sandblasting. However, variation of 11.3, 8.6 and 11.0 N for C1, C2 and C3 for interfacial failure loads were observed due to the heat treatment whilst application of a 2 way ANOVA showed no significant statistic variation $P < 0.05$.

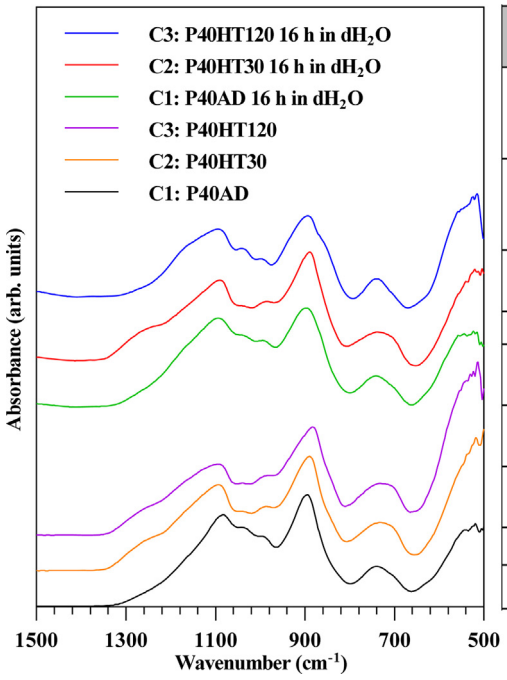

Wavenumber (cm^{-1})	Absorption Mode
1270<	Asymmetric stretching of the PO_2 O-P-O (Q^2)
1180-1170	Symmetric stretching of the PO_2 O-P-O (Q^2)
1105-1100	P-O^- chain terminators (Q^1)
1055	PO_3 end groups (Q^1)
1012	PO_3 symmetric stretching
912-887	Asymmetric stretching of the P-O-P
769-746	Symmetric Stretching P-O-P (Q^1 units)
565-500	PO^- or PO_4^{3-} (Q^0 units)
560	Hematite Fe_2O_3

Fig. 2. IR absorption spectra for as manufactured coatings and coatings 16 h post degradation in dH_2O. (Insert table) attributed IR absorption modes.

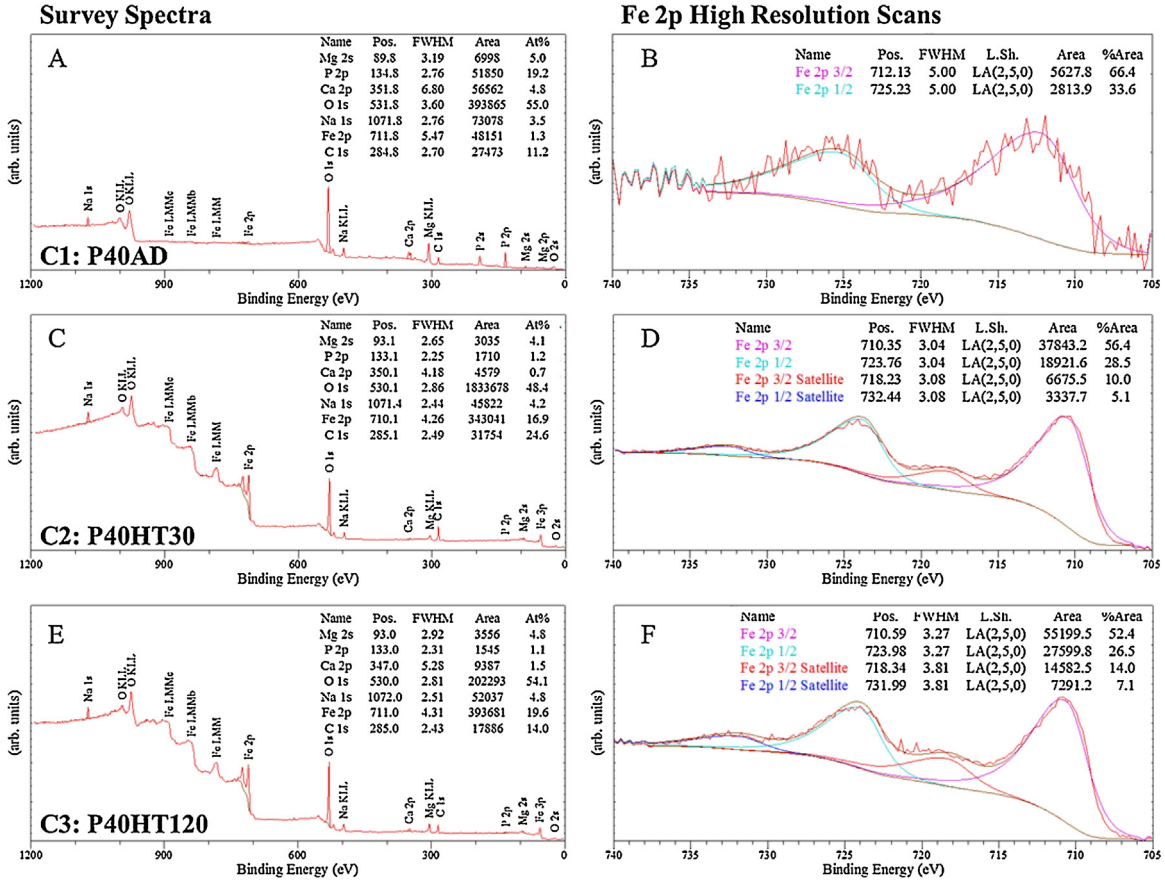

Fig. 3. XPS survey spectra and high-resolution spectra of Fe 2p. (A) C1: P40AD survey (B) C1: P40AD Fe 2p. Broad peak positions suggested multiple oxidation states associated with Fe following deposition (C) C2: P40HT30 survey (D) C2: P40HT30 Fe 2p (E) C3: P40HT120 survey (F) C3: P40HT120 Fe 2p. (D and F) Following C2: P40HT30 and C3: P40HT120 the coating surfaces were phosphorous deficient whilst the location of the Fe 2p spectral peaks suggested the prominence of Fe_2O_3.

Table 2
Surface compositions determined by XPS of C1: P40AD, C2: P40HT30 and C3:P40HT120. Column (at%) and column (*at%) show the normalised compositions without the contribution of adventitious carbon and the absolute quantification including the carbon C 1s emission respectively.

	C1: P40AD			C2: P40HT30			C3: P40HT120		
	mol%	at%	*at%	mol%	at%	*at%	mol%	at%	*at%
(P 2p) P_2O_5/Phosphorous	44.1	21.6	19.2	3.8	1.6	1.2	2.9	1.3	1.1
(Na 1s) Na_2O/Sodium	8.2	4.0	3.5	12.9	5.5	4.2	12.5	5.6	4.8
(Ca 2p) CaO/Calcium	22.0	5.4	4.8	5.2	1.0	0.7	8.0	1.8	1.5
Mg (2s) MgO/Magnesium	22.9	5.6	5.0	25.4	5.4	4.1	25.8	5.6	4.8
(Fe 2p) Fe_2O_3/Iron	2.9	1.4	1.3	52.7	22.4	16.9	50.8	22.8	19.6
(O 1s) Oxygen	–	62.0	55.0	–	64.1	48.4	–	62.9	54.1
(C 1s) Carbon	–	–	11.2	–	–	24.6	–	–	14.0

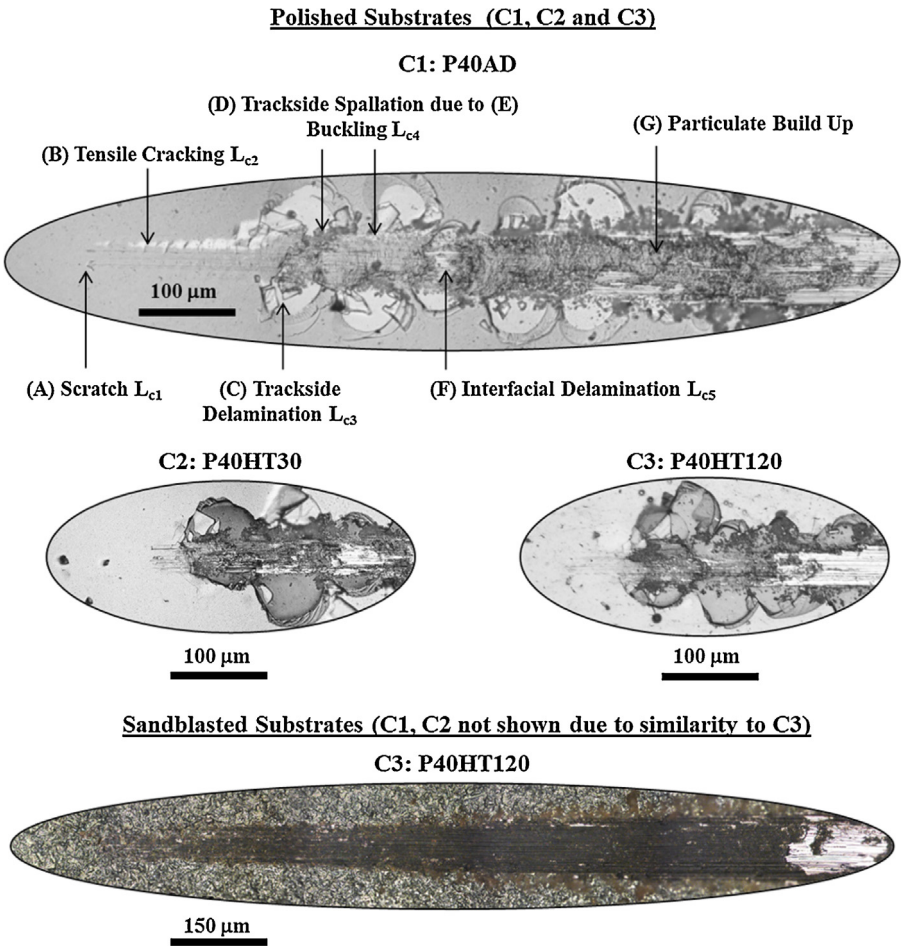

Fig. 4. Scratch adhesion testing of C1: P40AD, C2: P40HT30 and C3: P40HT120. The characteristic wear mechanisms have been labelled in C1: P40AD as (A) Scratch L_{c1}, (B), Tensile cracking L_{c2}, (C) Trackside delamination L_{c3}, (D) Trackside spallation due to buckling L_{c4}, (F) Interfacial delamination L_{c5}, (G) Particulate build Up.

3.2.2. *Pull off testing*

The interfacial mechanical strengths of C1, C2, and C3 were assessed by tensile pull off testing. As a control, the epoxy was used to glue a stub to a Ti6Al4V substrate (Fig. 6C). In all pull off cases ($n = 8$) during testing of the epoxy, failure occurred cohesively at an average load of ≈76.8 MPa. The failure loads ranged from a (≈59.2–87.2 MPa). Coatings C1: P40AD, C2: P40HT30 and C3: P40HT120 failed at ≈79.3, 78.6 and 73.6 MPa respectively showing ranges (60.8–105.6), (64.0–99.2) and (70.4–80.8) MPa. Microscopic observation of the failure location suggested epoxy cohesive failure in all cases. For comparative purposes (Fig. 6 *insert "Coating Failure"*) represents the complete interfacial failure a of 490 nm thick silicate glass coating (SiO_2-50 CaO-31 Na_2O-17 P_2O_5-2 mol%), which was observed to fail at 14.0 ± 1.0 MPa with a range of (8.8–17.6 MPa).

FIB-SEM cross sections (Fig. 6A-C) were milled through the coating/substrate interface to observe through thickness alterations of the coating features due to heat treatment. C1: P40AD (Fig. 6A, D) followed the topographical features of the substrate and demonstrated complete interfacial adherence. Partial coating void formation and delamination was observed for C2: P40HT30 (Fig. 6B, E). C3: P40HT120 showed consistent delamination of the coating along the interface on both polished and sandblasted substrates (Fig. 6C, F).

3.3. *Degradation and ion release*

Coatings C1: P40AD, C2: P40HT30 and C3: P40HT120 were degraded in dH_2O for up to 96 h (Fig. 7B). Degradation profiles of C1: P40AD revealed an initial exponential profile in the first

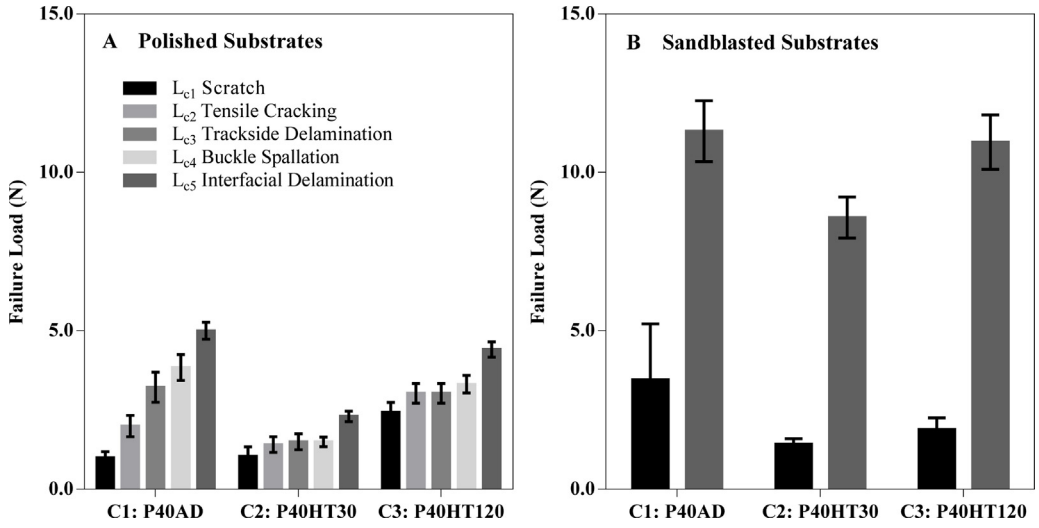

Fig. 5. Scratch adhesion testing of C1: P40AD, C2: P40HT30 and C3: P40HT120. Scratch test critical loads and failure mechanisms for coatings on (A) Polished Ti6Al4V, (B)Sandblasted Ti6Al4V.

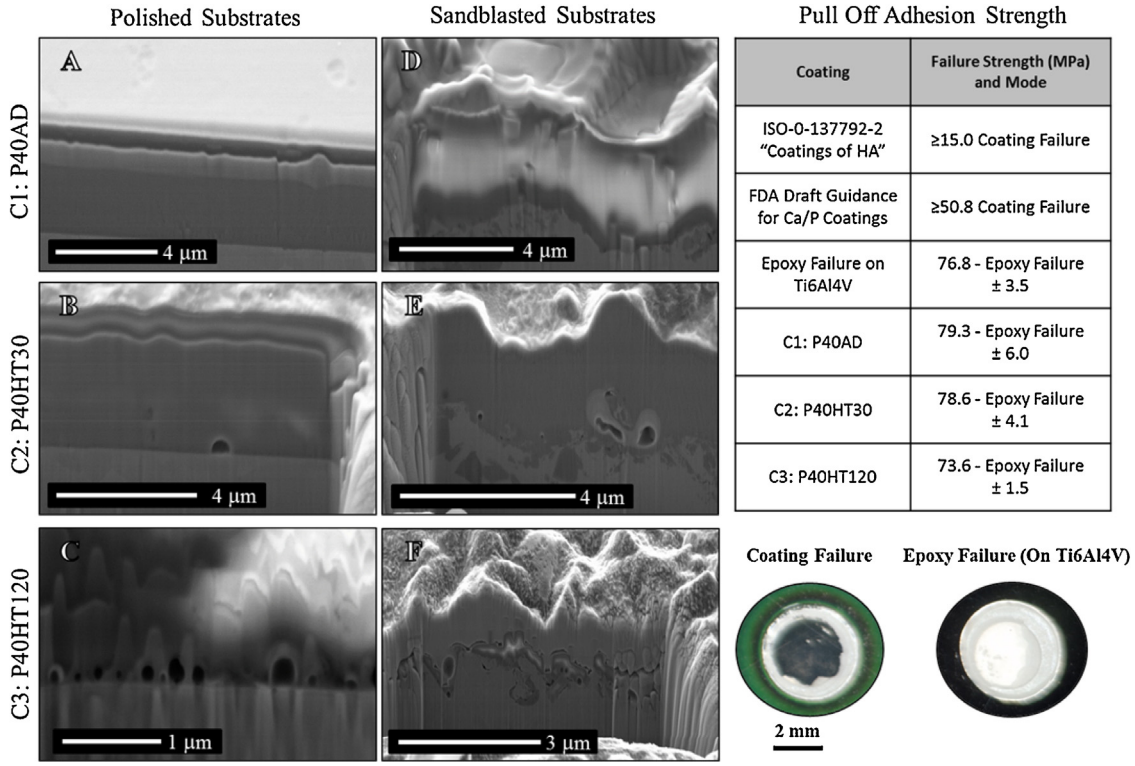

Pull Off Adhesion Strength

Coating	Failure Strength (MPa) and Mode
ISO-0-137792-2 "Coatings of HA"	≥15.0 Coating Failure
FDA Draft Guidance for Ca/P Coatings	≥50.8 Coating Failure
Epoxy Failure on Ti6Al4V	76.8 - Epoxy Failure ± 3.5
C1: P40AD	79.3 - Epoxy Failure ± 6.0
C2: P40HT30	78.6 - Epoxy Failure ± 4.1
C3: P40HT120	73.6 - Epoxy Failure ± 1.5

Fig. 6. (Table insert) Tensile failure loads and respective failure modes for C1: P40AD, C2: P40HT30 and C3: P40HT120. All coating strengths exceeded the strength of the epoxy. FIB SEM cross sectional micrographs. Polished and Sandblasted (A, D) C1: P40AD, complete interfacial adherence, (B, E) C2: P40HT30, isolated delamination, (C, F) C3:P40HT120, consistent delamination along the substrate/coating interface.

Table 3
Dissolution and ion release rates in distilled and ultra-pure water respectively. Dissolution rates were calculated between 2–24 h and 2–96 h whilst ion release rates were calculated between 2–24 h for C1: P40AD, C2: P40HT30 and C3: P40HT120. Ion release however was continued to the 48 h time point in Fig. 7.

	2 h	2–24 h	2–96 h	Ion release (PPM h^{-1}) (r^2) 2–24 h				
	$\times 10^{-4}$ mg mm^2	($\times 10^{-4}$ mg mm^2 h^{-1}) (r^2)		Na	Mg	P	Ca	Fe
C1: P40AD	2.9 ± 0.4	2.05 ± 0.35 (0.92)	Fully degraded by 48 h	0.08 ± 0.01 (0.98)	0.08 ± 0.01 (0.98)	0.34 ± 0.1 (0.94)	0.07 ± 0.02 (0.95)	0.05 ± 0.02 (0.89)
C2: P40HT30	0.7 ± 0.3	0.61 ± 0.10 (0.93)	0.68 ± 0.02 (0.99)	0.02 ± 0.01 (0.92)	0.02 ± 0.00 (0.99)	0.10 ± 0.00 (0.99)	0.02 ± 0.00 (0.99)	0.01 ± 0.00 (0.99)
C3: P40HT120	0.3 ± 0.1	0.85 ± 0.06 (0.99)	0.84 ± 0.01 (0.99)	0.02 ± 0.01 (0.72)	0.02 ± 0.00 (0.99)	0.10 ± 0.01 (0.99)	0.02 ± 0.01 (0.85)	0.01 ± 0.00 (0.92)

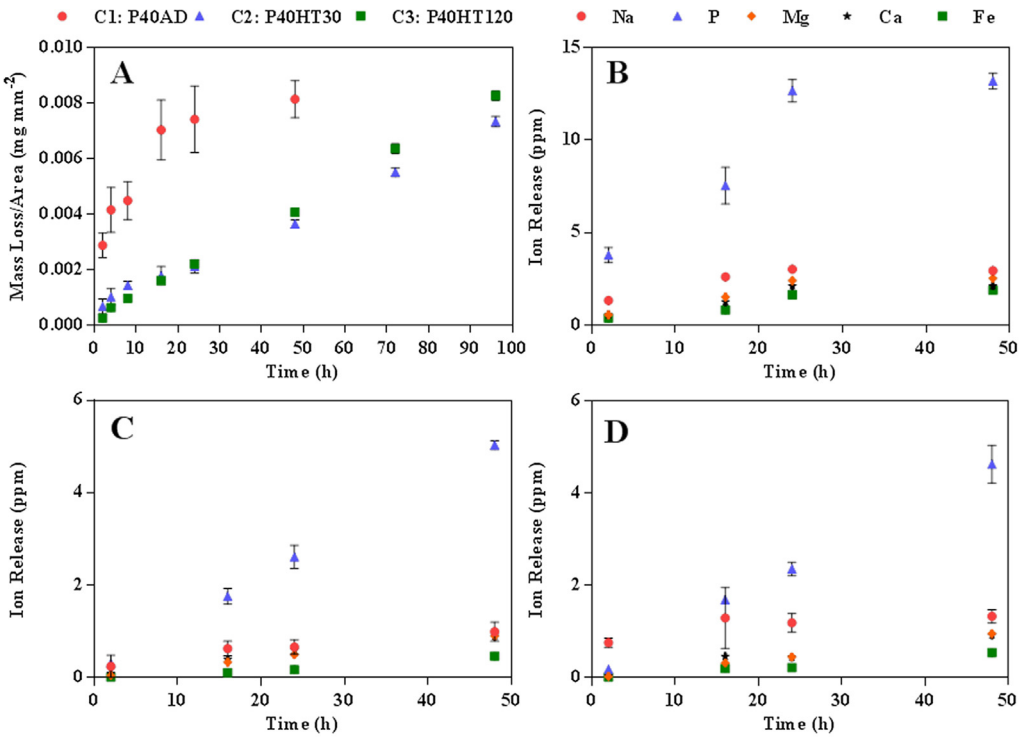

Fig. 7. Degradation of coatings C1: P40AD, C2: P40HT30 and C3: P40HT120. (A) Dissolution rates up to 96 h in distilled water and Ion release profiles following dissolution in ultra-pure water up to 48 h (B) C1: P40AD (C) C2: P40HT30 and (D) C3: P40HT120.

2 h of degradation followed by a linear profile from 2 to 24 h (Fig. 7A). By the 2 h time point the comparative mass losses were (2.9, 0.7 and 0.3) $\times 10^{-3}$ mg mm^{-2} for C1, C2, and C3 respectively, suggesting an increased stability in the first 2 h of degradation due to heat treatment (Fig. 7A). From 2 to 24 h degradation rates were (2.1. 0.6 and 0.9) $\times 10^{-4}$ mg mm^{-2} h^{-1} respectively (Fig. 7A). C1: P40AD was fully resorbed by the 48 h time point. Continued degradation up to 96 h of C2: P40HT30 and C3: P40HT120, followed similar degradation profiles, degrading at rates of (0.7 and 0.8) $\times 10^{-4}$ mg mm^{-2} h^{-1} (Fig. 7A). Linear regression r^2 values ranged from 0.92 to 0.99 supporting a linear correlation. See Table 3 for comparative dissolution rates.

Linear ion release profiles were observed for all coatings and ions of Na, P, Mg, Ca and Fe over the 48 h time period in ultra-pure water with the exception of C1: P40AD which was fully resorbed by the 48 h time point. Therefore ion release slopes were calculated from 2 to 24 h. r^2 values ranged from 0.85 to 0.89 with the exception of C3: P40HT120 which had an outlier at 16 h for Na release.

For the three coatings the ion release rates ranked P > Na > Mg > Ca > Fe whilst the observed exponential degradation profile for C1: P40AD was reflected by the initial surge of ions released by the 2 h time point (Fig. 7B).

Ion release rates ranged from 0.08 to 0.05 ppm h^{-1}, 0.01–0.02 ppm h^{-1} and 0.01–0.02 ppm h^{-1} for C1, C2 and C3. Heat treatment led to a reduction in ion release rates by factors of (4.0, 3.6)-Na (4.1, 4.3)-Mg (3.7, 3.9)-P (3.0, 3.4)-Ca and (7.7, 5.4)-Fe for C2: P40HT30 and C3: P40HT120 respectively. See Table 3 for comparative ion release rates.

3.4. Surface topography

Electron micrographs of the coating surfaces pre and post heat treatments and pre and 16 h post degradation on both polished and sandblasted substrates have been presented in Fig. 8. In Fig. 8A, C1: P40AD showed no notable surface features. Following heat treatment of C2: P40HT30 the coating colour became blue/violet (Fig. 8B inset). (Fig. 8B, *C* for C2: P40HT30 and C3: P40HT120 polished, showed surface features, consistent with expansion and contraction of the surface layer during heating. Additionally expansion craters were observed to be dispersed across the coating surfaces. An increase in surface roughness from C1: P40AD to C2: P40HT30 and C3: P40HT120 was supported by AFM measurements (Fig. 8M) for which $n = 4400\ \mu m^2$ regions were chosen for analysis. Roughness Ra values increased from (8 to 27 to 44 nm) respectively for coatings on polished substrates. In contrast coatings deposited onto sandblasted substrates showed no remarkable surface changes or trends relating to Ra values of 519, 321, and 485 following heat treatment (Fig. 8G, H, I, M). Coatings on sandblasted substrates showed surface smoothing from the calculated substrate Ra value of 696 nm whilst no significant variation was observed from the polished substrate roughness of 7 nm. Notably, surface area analysis by AFM revealed that sandblasted substrates had an area of 18.5% greater than the projected 400 μm^2, leading to an 21.5% increase for C1: P40AD.

Randomly dispersed degradation pits were formed across all coatings following 16 h in dH_2O on polished substrates and sandblasted C1: P40AD. The pits were visually observed by SEM analysis (Fig. 8D, E, F, J, K, L). Pits formed in C1: P40AD penetrated to the depth of the substrate as suggested in (Fig. 8D). In contrast, degradation pits in C2: P40HT30 were interconnected and did not extend through the thickness of the coating by the 16 h immersion time point (Fig. 8E). Coatings on sandblasted substrates showed dissolution pitting following 16 h immersion for C1: P40AD whilst C2: P40HT30 and C3: P40HT120 showed morphological changes associated with uniform dissolution and, smoothing of the surface whilst degradation of C3: P40HT120 revealed holes formed beneath the surface (Fig. 8J, K, L).

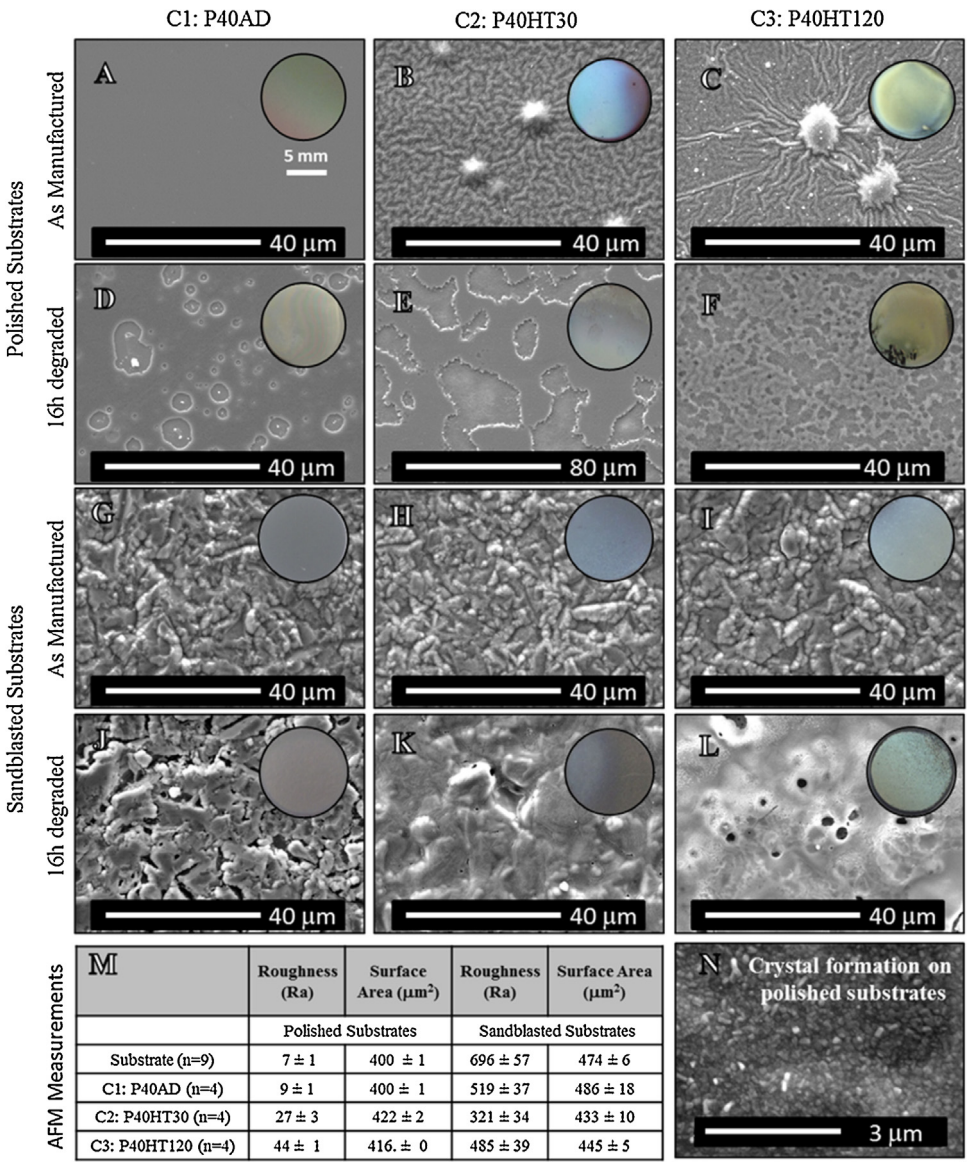

M	Roughness (Ra)	Surface Area (µm²)	Roughness (Ra)	Surface Area (µm²)
	Polished Substrates		Sandblasted Substrates	
Substrate (n=9)	7 ± 1	400 ± 1	696 ± 57	474 ± 6
C1: P40AD (n=4)	9 ± 1	400 ± 1	519 ± 37	486 ± 18
C2: P40HT30 (n=4)	27 ± 3	422 ± 2	321 ± 34	433 ± 10
C3: P40HT120 (n=4)	44 ± 1	416. ± 0	485 ± 39	445 ± 5

Fig. 8. Micrographs of coating surface pre and post degradation of as manufactured on polished substrates (A)(B)(C) on sand blasted substrates (G)(H)(I) and 16 h degradation on polished substrates (D)(E)(F) on sandblasted substrates (J)(K)(L) C1: AD C2: P40HT30 C3: P40HT120 respectively. (M) AFM roughness and surface area measurements (N) Hematite crystals formed at P40HT120 on polished substrates.

4. Discussion

4.1. Composition and structural analysis by EDX, XPS, FTIR, and XPS

A post annealing stage in glasses is conventionally conducted within the processing window, defined as the range from glass transition temperature to the onset of crystallisation. Such treatment should allow residual stresses formed during quenching to diffuse from the glass, therefore leading to improved mechanical properties due to molecular relaxation [42].

PBG's are amorphous, covalently bound solids, composed of a polymeric like backbone of phosphate tetrahedral PO_4. The inclusion of ionic species depolymerises the network and enhances durability via network cross linking [43,44]. Previous research showed that compositionally equivalent sputtered coatings were structurally different to their melt quenched counterparts, showing increased polymerisation of the bulk material which was confirmed via ^{31}P NMR and XPS [31,35]. This increase in polymerisation led to greater solubility of sputtered coatings [31,35]. Therefore the aim of this study was to observe the effects of post deposition annealing (PDA) on the mechanical and solubility behaviour of PBG coatings.

The XRD results suggested that C1: P40AD was deposited amorphous. Following the heat treatments of C2: P40HT30 and C3: P40HT120 the formation and subsequent growth of Hematite crystals within an amorphous matrix was observed. A low intensity peak for Hematite was located around 33° 2θ following C2: P40HT30 and C3: P40HT120. The broad hump associated with amorphous diffraction remained, suggesting the formation of a glass-ceramic structure. This was supported by IR absorption (Fig. 2) revealing peaks located between 500 and 565 cm^{-1}; consistent with PO_4^{3-} within the phosphate structure and the possible presence of Hematite. Wang et al. reported vibration bands for a Hematite (α-Fe_2O_3) standard between 567 and 584 cm^{-1}. The increased IR peak intensity in C2: P40HT30 and C3: P40HT120 in comparison to the C1: P40AD supported the growth of Hematite crystals [37].

Fig. 9 depicts the diffusion mechanisms and oxidation interactions observed during heat treatment. The XPS surface analysis

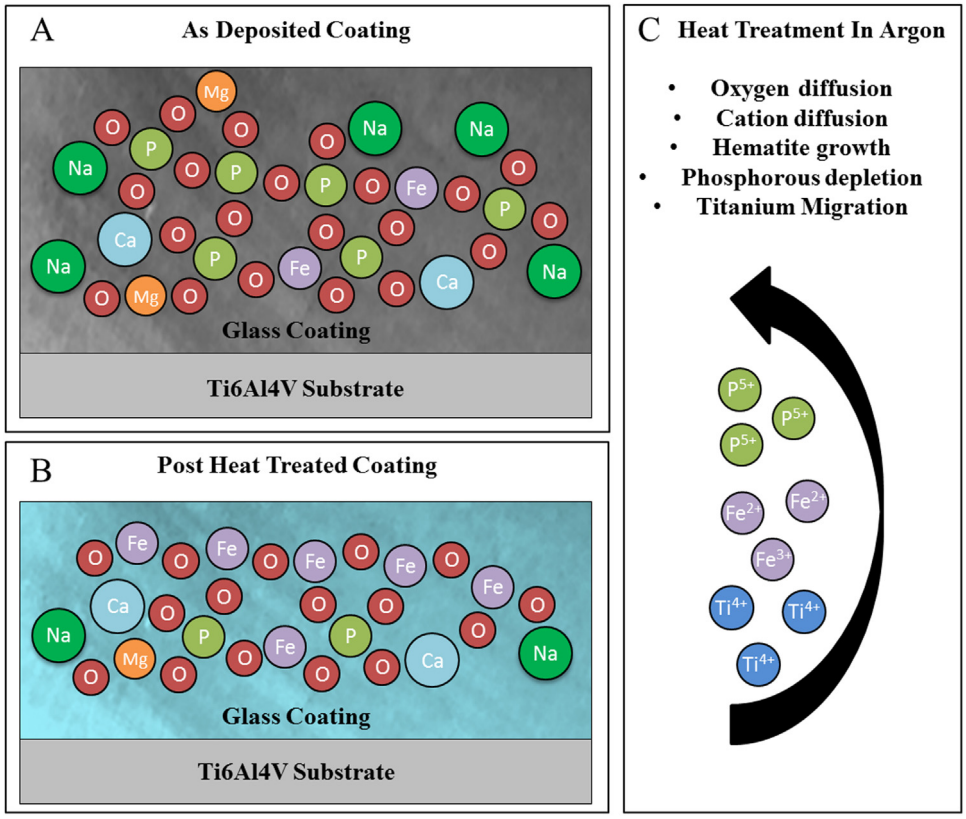

Fig. 9. Diagram depicting suggested structural and compositional changes from (A) C1: P40AD to (B) C2/C3:P40HT30/120 following heat treatment. (C) Migration of cations, phosphorus depletion and growth of Hematite.

showed no peaks associated with phosphorus following C2: P40HT30 and C3: P40HT120 whilst the proportion of Fe increased from 1.4% to 22.4% and 22.8% (see Table 2 and Fig. 3A, C, E). The volatility of phosphorous may have led to a surface deficiency [45]. Boyd et al. suggested that for Ca:P films which underwent post deposition annealing at 500 °C, the Ca:P was reported to increase, explained by volatile phosphorous evaporating from the surface at lower annealing temperatures [46]. From XPS, the broad spectral range of the Fe 2p peak in C1: P40AD suggested that Iron on the surface (0–10 nm) may have existed in multiple oxidation states, FeO, Fe_2O_3, Fe_3O_4 and FeOOH which was the cause of broadening of the Fe 2p high resolution spectra (see Fig. 3B) [41]. FeOOH, however was not supported as hydroxyl groups were absent from all IR spectra (see Fig. 2). Following C2: P40HT30 and C3: P40HT120, the defined peak shift towards the lower binding energies of 710.4 and 710.6 eV combined with the relative distances between the main spectral peaks and satellite peaks suggested the prominence of Fe_2O_3 (see Fig. 3D, F) [39,41].

The complementary techniques of FTIR, XPS, and XRD confirmed Iron oxidation on the surface and the crystallisation of Fe_2O_3 as Hematite. SEM imaging at 64,000 times magnification showed crystallite growths (Fig. 8N). As depicted in Fig. 9, diffusion of cations into the bulk glass during annealing may have promoted the migration of $Fe^{2+and3+}$ ions into the vacancy sites [47]. Minitti et al. reported the formation of <1 μm thick Hematite coatings on oxidised basaltic glass at 700 °C whilst showing no such formation at 350 °C [36]. The mechanism was believed to be the removal of electrons from Fe^{2+} by oxidation and re-oxidation at the surface with Fe to form Fe^{3+} similar to the effect observed here. As suggested by Cook and Cooper et al. for Iron containing silicate glass, migration of oxygen allows outward migration of Fe to fill the electron holes in the surface material leading to the growth of Hematite observed here [47,48]. Wisniewski et al. demonstrated the formation of Hematite and Magnetite crystals in Iron containing soda-lime glass when annealed at 480 °C (30 °C below the measured T_g of 510 °C) [49]. This migration of oxygen to the surface could have caused the observed craters formed post heat treatment (Fig. 8B and C).

Colour changes of the samples to bluish/violet in Fig. 8 inserts following heat treatment may have been due to a redox reaction between the Ti6Al4V substrate and oxygen within the glass [50,51]. This interference effect as the oxide layer grew was also observed by Kumar et al. for Ti6Al4V surfaces heat treated at 500 °C [52].

4.2. Adhesion and mechanical properties

Magnetron sputtering enabled film deposition into the topography of the substrate, leading to enhanced adhesion [53,54]. Such adherence has been observed via FIB-SEM interfacial observation of deposited phosphate glasses on Ti6Al4V substrates [35]. Coating thickness variation from C1: P40AD was recognised from light interference fringe patterns as visible light reflected off the substrate and through the sample (Fig. 8A). Analysis of coating thickness by SEM cross section indicated a standard error of 90 nm for ($n = 5$) locations across a sample. Ideally, to minimise variation, the sample should be rotated uniformly with respect to the plasma. The capabilities of the specific rig design used for this deposition did not allow for sample rotation.

The scratch test and pull off adhesion tests describe the failure mechanisms of a coating under multi-axial and tensile loads respectively [55]. The scratch test is considered the more versatile method of determining mechanical adherence of the coating as it provides multiple failure modes. Failure characteristics are more representative of practical orthopaedic applications as coating fail-

ures may more often be caused by shear, rather than pure tension. The limitation of the pull off method is the tensile strength of the epoxy, however it remains the standardised quantitative assessment of coating/substrate mechanical strength. ISO-0-137792 Part 2 "Coatings of Hydroxyapatite" states that the minimum interfacial tensile strength should be no less than 15.0 MPa. Callahan et al. stated in the 1994 FDA draft guidance for Ca/P coatings on medical implants that the minimum interfacial strength approved for FDA commercially approved coatings was 50.8 MPa (Fig. 6A) [56,57].

Interfacial integrity of coatings on polished substrates following heat treatment, in the case of C2: P40HT30 and C3: P40HT120 appeared to be compromised by coating/substrate delamination; as observed in FIB-SEM cross sections (see Fig. 6B and C). Scratch tests showed variation in L_{c5} (interfacial delamination) from 5.0 to 2.3 to 4.4 N for C1, C2 and C3 respectively. The failure modes for L_{c1}-L_{c5} ranged over a 4.0 N for C1: P40AD, and were, in contrast, closely spaced ranging over 1.3 and 2.0 N for C2: P40HT30 and C3: P40HT120 demonstrating a decrease in ductility due to catastrophic coating failure at the point of initial indentation $L_{c1.}$ C3: P40HT120, showed increased L_{c1} (initial scratch) to 2.0 N and L_{c5} to 4.4 N. All coatings exhibited brittle failure mechanisms however heat treatment seemingly led to increased brittleness and hardness with prolonged dwell time of 120 min.

Coatings on sandblasted substrates showed no signs of catastrophic failure, specifically the absence of spallation due to trackside delamination. The interfacial properties were improved as delamination occurred at 8.6–11.3 N for C1, C2 and C3 respectively (B). Toque et al. applied up to 2.5 N loads on 1.3–2.0 μm Ca/P sputtered films deposited onto 316 L stainless steel and their results showed interfacial delamination at 800–900 mN. Post deposition annealing similarly led to a reduction in interfacial failure loads as shown here for polished substrates, in the range of 450–550 mN [54]. Additionally Cheng et al. compared pull off and scratch tests of sol gel HA coatings on Ti6Al4V and reported scratch delamination of up to 487 mN and pull off strengths of up to 22 MPa [58].

The measurable interfacial failure strength at the coating substrate interface is considerably lower than the anticipated tensile properties of the glass itself to fail cohesively in tension. Cozien-cazuc et al. tested the tensile properties of MQ: P40 formed as glass fibres, both as prepared and up to 3 d degradation in distilled water and reported tensile strengths of 480 ± 150, decreasing to 370 ± 60 MPa. Following annealing at 444 °C (5 °C below the T_g) a reduction in tensile strength to 290 ± 50 MPa was observed and an increase in strength following 3 d degradation to 460 ± 140 MPa [59]. For coatings on polished substrates a similar reduction in failure properties due to coating embrittlement was also observed following annealing. Sglavo et al. also showed ranging tensile properties of PBG optical fibres of between 200 and 400 MPa [60].

All coatings prepared and tested here showed sufficient minimum adhesive properties according to ISO and FDA regulations on pull off testing (Fig. 6); the actual failure loads however were unattainable due to limitations of the epoxy glue used. Ong et al. tested ion beam sputtered Ca:P films comparing the pull off strength of deposited amorphous, water quenched and furnace cooled coatings and reported pull of strengths of 38.0 ± 8.2 MPa, 17.0 ± 6.5 MPa and 9.0 ± 9.0 MPa respectively with failure either occurring at the coating interface or cohesively [61]. 45S5 Bioglass has been plasma sprayed with little success as failure was shown to occur from thermally induced residual stresses at the Ti coating interface with adhesion strength of approximately 8.56 ± 0.57 MPa [25]. The use of a bonding coat (60 wt% Al_2O_3 40 wt% TiO_2) to accommodate the thermal expansion coefficient (TEC) mismatch of Bioglass and the substrate, improved bonding strength to 27.17 ± 2.24 MPa with failure otherwise occurring by coating delamination [25].

Similar studies reporting pull off values were also performed by Mardare et al. and Stan et al. who produced silicate bioactive glasses by sputtering. Mardare et al. reported adhesion strength of 41.0 ± 4.5 MPa for 300 nm bioactive glass on titanium substrates. Post-deposition heat treatment of the coating layer at 900–1000 °C caused crystallisation and subsequent reduction in adhesion to 16.3 ± 1.9 MPa [28]. Mardare's work was conducted above the phase transition temperature of titanium in which the titanium changes from HCC to BCC structure and reduces in volume, inducing stress in the materials [28,62].

Stan et al. reported pull off interfacial strengths of as deposited silicate glass coatings of 29.2 ± 7.0 MPa and attributed less than optimal adhesion to the TEC mismatch between deposited coatings and substrates during deposition [63]. Improvements in adhesion by reducing the TEC of the coating through compositional changes led to production of a glass coating with TEC of $10 \times 10^{-6}\ K^{-1}$, applied to titanium substrates with TEC of $9.2–9.6 \times 10^{-6}\ K^{-1}$ [64]. The adhesion strength for this glass was measured as >75 MPa (limited by the epoxy) [65]. Whilst bonding was dramatically improved by tailoring TEC by altering composition, this restricted the flexibility of coating compositions that could be applied. Further publications demonstrated improved pull off to >85.0 MPa (again limited by the strength of the epoxy) following an annealing process during which Stan et al. suggested that heat treatment caused a noticeable diffusion of titanium into the glass at the interface, forming chemical bonding leading to improved adhesion [29]. Additionally exploration of graded buffer layers proved to be effective methods for adhesive strengthening [29,63,66,67].

TEC could not be assessed in thin films; therefore the MQ5: P40 Fe4 was cast as rods for comparison and measured as $13.6 \pm 0.2 \times 10^{-6}\ K^{-1}$. These values however are not directly comparable as it was previously shown that structures and thermal properties varied in coatings and melt quenched glasses. Elmer et al. cited TEC in TI6Al4V between 8.5 and $10.0 \times 10^{-6}\ K^{-1}$ [68]. The higher TEC of PBG with respect to the Ti6Al4V substrate may have caused the observed ripples in the coating shown in SEM micrographs (Fig. 8B, C) and the interfacial delamination shown in FIB-SEM sections (Fig. 6B, C, E, F) following C2: P40HT30 and C3: P40HT120.

4.3. Degradation and ion release

Degradation of PBG occurs by hydration during which H^+ ions interchange with cations to form P-OH^- and subsequent disentanglement of the polymer like chains by hydrolysis [69,70]. The as deposited PBG coating; C1: P40AD, was found to be highly soluble in the first 2 h, degrading exponentially, prior to stabilising to a linear regime thereafter [35] as observed in Fig. 7A. However the thermal annealing processes led to a reduction in initial solubility as the comparative mass losses were 2.9, 0.7 and 0.3×10^{-3} mg mm^{-2} at the 2 h time point for C1, C2 and C3 respectively. This effect may have been due to reoxidation of Iron as Fe^{3+} to form hydration resistant Fe-O-P bonds and the reduction of soluble P-O-P bonds following heat treatment at the surface of the material as shown by XPS (Fig. 3B, C) [18,35,47].

The formation of Hematite crystals and Iron oxidation led to improved bulk durability over the 96 h time period. From 2 h to 96 h the linear degradation rates for C2: P40HT30/C3: P40HT120 and C1: P40AD were 0.68 ± 0.02, 0.84 ± 0.01 and $2.05 \pm 0.35 \times 10^{-4}$ mg mm^{-2} h^{-1} respectively, showing an increase in coating durability by a factor of $2.44–3.01 \pm 0.35$. There were, however, no significant variations in the quantitative degradation properties between the different lengths of heat treatment, C2: P40HT30 and C3: P40HT120. Surface micrographs of C1: P40AD showed randomly distributed narrow corrosion pits 16 h post degradation. Following C1: P40HT30, corrosion pits appeared to

widen and following C3: P40HT120 visible pitting associated with degradation was fairly uniform, indicating that prolonged heat treatment led to a more diffused, homogenous bulk structure. Chouka et al. and Cozien-Cazuc et al. both showed pitting corrosion of Ca:P and PBG fibres following degradation in Tris-Buffered HCl and distilled water respectively, whilst also reporting improved durability of annealed fibres. Chouka et al. also suggested that durability was proportional to annealing temperature [71,72].

The effects of ion release for Ca, P, Mg, and Fe on therapeutic potential have been reported [73–77]. For Ca^{2+} 2–8 mM (80–320 PPM) was deemed sufficient to facilitate osteoblast proliferation, whilst 6–8 mM (240–320 PPM) was reported as optimal, causing cytotoxicity above 10 mM (400 PPM) [73]. Phosphate ion concentrations from 2–10 mM (62–310 PPM) were found to stimulate gene expression for osteoblast differentiation [74]. He et al. reported that Mg^{2+} from 1 to 3 mM (24–73 PPM) improved osteoblast cell viability, alkaline phosphatase and osteocalcin expression [75]. A toxic limit for Fe was reported as 0.4 mM (22 PPM) [76]. Sondi et al. demonstrated the antimicrobial effectiveness of Ag nano particles on *E. coli*, using 10–60 $\mu g\,cm^{-3}$ (0.01–0.06 PPM), showing 70–100% growth inhibition [77]. In comparison Figure 7 showed that cumulative ion release by 48 h in 15 ml of ultra-pure water ranged in C1: P40AD, C2: P40HT30 and C3: P40HT120, from (1–3), (5–13), (1–3), (1–2) and (1–2) PPM for Na, P, Mg, Ca and Fe respectively. However for accurate comparison of ion release effects, consideration of liquid volumes should be carefully considered along with the media used for testing. For example, dissolution volumes vary from μl to ml during in vitro studies of MG63 Osteoblast cells, often with working volumes of 0.2–0.3 ml, therefore ion concentrations could be up to 75× higher as compared to the 15 ml used here, providing sufficient ionic concentrations for therapeutic efficacy.

Production of PBG thin films has been shown to be a promising method for delivering a controlled release of ions at a dissolution site, whilst the ability to further control such properties through heat treatment has been confirmed.

These findings represent a step forward in understanding the mechanical and degradation properties of fully resorbable PBG coatings, intended for application on orthopaedic implants to facilitate osseointegration. The ability to incorporate a range of therapeutic ions using the magnetron sputtering process could lead to a stratified approach to promoting orthopaedic implant integration.

5. Conclusions

RF magnetron sputtered PBG coatings were deposited amorphous onto both polished and sandblasted Ti6Al4V substrates. Coatings were subsequently heat treated for dwell times of 30 and 120 min at 500 °C. Similar structural changes were observed for P40HT30 and P40HT120, associated with the formation of Fe_2O_3 Hematite crystals whilst XPS showed the reduction of phosphorous from (21.6–1.3) at%, coupled with an increase in Iron from (1.4–22.8) at% within the surface layers.

Pull off adhesion tests were limited by the strength of the epoxy, therefore all coatings showed average strengths in excess of 73.6 MPa, exceeding the international ISO standard and FDA requirements. Scratch adhesion tests revealed brittle failure modes for coatings on polished substrates. Although heat treatment improved the overall adhesion values, coatings failed catastrophically at the location of initial indentation, suggesting that heat treatment led to increased hardness at the expense of coating embrittlement. In contrast coatings applied to sandblasted substrates were mechanically durable, showing no trackside delamination or tensile cracking whilst loads associated with interfacial delamination were increased to between 8.6 and 11.3 N however variation due to heat treatment was not statistically significant.

Coatings on sandblasted substrates were degraded in dH_2O for up to 96 h and assessed for ion release in ultrapure water up to 48 h. C1: P40AD was fully resorbed beyond 24 h, heat treated coatings remained beyond the 96 h time point. Heat treatment improved the durability of coatings by stabilising the initial $t^{1/2}$ solubility profile in the first 2 h of submersion and ultimately reduced linear degradation rates by 2.4–3.0 ± 0.35 for C2: P40HT30 and C3: P40HT120 respectively. Heat treatment led to a reduction in ion release rates by maximum factors of 3.9, 4.0, 4.3, 3.4 and 7.7 for P, Na, Mg, Ca and Fe respectively. Release rates ranged from 0.08 to 0.05 ppm h^{-1}, 0.01–0.02 ppm h^{-1} and 0.01–0.02 ppm h^{-1} for the C1: P40AD, C2: P40HT30 and C3: P40HT120 coatings respectively.

Acknowledgements

This work was supported by the Engineering and Physical Sciences Research Council [grant number EP/K029592/1]; and the Centre for Innovative Manufacturing in Medical Devices (MeDe Innovation). The authors would like to gratefully acknowledge Saul Vazquez Reina for assistance with ICP-MS analysis and Dr. Emily Smith for reviewing the XPS results as well as the Nanoscale and Microscale Research Centre at the University of Nottingham for SEM access.

References

[1] M. Navarro, A. Michiardi, O. Castano, J.A. Planell, Biomaterials in orthopaedics, J R Soc Interface 5 (27) (2008) 1137–1158.
[2] S. Zhang, Biological and Biomedical Coatings Handbook Processing and Characterization, CRC Press, Florida, 2011.
[3] B. Clarke, Normal bone anatomy and physiology, Clin. J. Am. Soc. Nephrol. 3 (Suppl 3) (2008) S131–S139.
[4] E. Jimi, S. Hirata, K. Osawa, M. Terashita, C. Kitamura, H. Fukushima, The current and future therapies of bone regeneration to repair bone defects, Int. J. Dentist. 2012 (2012).
[5] J. Sieniawski, W. Ziaja, K. Kubiak, M. Motyka, Microstructure and mechanical properties of high strength two-phase titanium alloys, Titanium Alloys-Advances in Properties Control (2013) 69–80.
[6] R.D. Bloebaum, D. Beeks, L.D. Dorr, C.G. Savory, J.A. DuPont, A.A. Hofmann, Complications with hydroxyapatite particulate separation in total hip arthroplasty, Clin. Orthop. Relat. Res. 298 (1994) 19–26.
[7] National Joint Registry. England, Wales and Northern Ireland, 2013.
[8] K. Mediaswanti, C. Wen, E.P. Ivanova, C. Berndt, F. Malherbe, V. Pham, J. Wang, A review on bioactive porous metallic biomaterials, J. Biomim. Biomater. Tissue Eng. 18 (104) (2013) 2.
[9] I. Ahmed, A. Parsons, A. Jones, G. Walker, C. Scotchford, C. Rudd, Cytocompatibility and effect of increasing MgO content in a range of quaternary invert phosphate-based glasses, J. Biomater. Appl. 24 (6) (2010) 555–575.
[10] E.A.A. Neel, W. Chrzanowski, S.P. Valappil, L.A. O'Dell, D.M. Pickup, M.E. Smith, R.J. Newport, J.C. Knowles, Doping of a high calcium oxide metaphosphate glass with titanium dioxide, J. Non-Cryst. Solids 355 (16) (2009) 991–1000.
[11] A. Hoppe, N.S. Guldal, A.R. Boccaccini, A review of the biological response to ionic dissolution products from bioactive glasses and glass-ceramics, Biomaterials 32 (11) (2011) 2757–2774.
[12] E.A.A. Neel, W. Chrzanowski, D.M. Pickup, L.A. O'Dell, N.J. Mordan, R.J. Newport, M.E. Smith, J.C. Knowles, Structure and properties of strontium-doped phosphate-based glasses, J. Roy. Soc. Interface (2008), rsif.2008.0348.
[13] J. Massera, L. Petit, T. Cardinal, J.-J. Videau, M. Hupa, L. Hupa, Thermal properties and surface reactivity in simulated body fluid of new strontium ion-containing phosphate glasses, J. Mater. Sci. Mater. Med. 24 (6) (2013) 1407–1416.
[14] D.S. Brauer, M.N. Anjum, M. Mneimne, R.M. Wilson, H. Doweidar, R.G. Hill, Fluoride-containing bioactive glass-ceramics, J. Non-Cryst. Solids 358 (12–13) (2012) 1438–1442.
[15] A. Kiani, N.J. Lakhkar, V. Salih, M.E. Smith, J.V. Hanna, R.J. Newport, D.M. Pickup, J.C. Knowles, Titanium-containing bioactive phosphate glasses, Philos. Trans. Series A Math. Phys. Eng. Sci. 370 (1963) (2012) 1352–1375.
[16] T. Kasuga, T. Hattori, M. Niinomi, Phosphate glasses and glass-ceramics for biomedical applications, Phosphor. Res. Bull. 26 (0) (2012) 8–15.
[17] T. Kasuga, T. Fujimoto, Y. Hosoi, M. Nogami, Calcium phosphate invert glasses and glass-ceramics with apatite-forming ability, Bioceramics 15 (240-2) (2003) 265–268.

[18] X.Y. Yu, D.E. Day, G.J. Long, R.K. Brow, Properties and structure of sodium-iron phosphate glasses, J. Non-Cryst. Solids 215 (1) (1997) 21–31.
[19] I. Ahmed, C.A. Collins, M.P. Lewis, I. Olsen, J.C. Knowles, Processing, characterisation and biocompatibility of iron-phosphate glass fibres for tissue engineering, Biomaterials 25 (16) (2004) 3223–3232.
[20] E.A. Neel, I. Ahmed, J. Pratten, S.N. Nazhat, J.C. Knowles, Characterisation of antibacterial copper releasing degradable phosphate glass fibres, Biomaterials 26 (15) (2005) 2247–2254.
[21] A.G. Avent, C.N. Carpenter, J.D. Smith, D.M. Healy, T. Gilchrist, The dissolution of silver-sodium-calcium-phosphate glasses for the control of urinary tract infections, J. Non-Cryst. Solids 328 (1–3) (2003) 31–39.
[22] I. Ahmed, D. Ready, M. Wilson, J.C. Knowles, Antimicrobial effect of silver-doped phosphate-based glasses, J. Biomed. Mater. Res. A 79 (3) (2006) 618–626.
[23] A. Al-Noaman, S.C. Rawlinson, R.G. Hill, Bioactive glass-stoichimetric wollastonite glass alloys to reduce TEC of bioactive glass coatings for dental implants, Mater. Lett. 94 (2013) 69–71.
[24] J. Gomez-Vega, E. Saiz, A. Tomsia, Glass-based coatings for titanium implant alloys, J. Biomed. Mater. Res. 46 (4) (1999) 549–559.
[25] G. Goller, The effect of bond coat on mechanical properties of plasma sprayed bioglass-titanium coatings, Ceram. Int. 30 (3) (2004) 351–355.
[26] G. Bolelli, V. Cannillo, R. Gadow, A. Killinger, L. Lusvarghi, J. Rauch, Microstructural and in vitro characterisation of high-velocity suspension flame sprayed (HVSFS) bioactive glass coatings, J. Eur. Ceram. Soc. 29 (11) (2009) 2249–2257.
[27] E. Mohseni, E. Zalnezhad, A.R. Bushroa, Comparative investigation on the adhesion of hydroxyapatite coating on Ti-6Al-4V implant: a review paper, Int. J. Adhes. Adhes. 48 (2014) 238–257.
[28] C.C. Mardare, A.I. Mardare, J.R.F. Fernandes, E. Joanni, S.C.A. Pina, M.H.V. Fernandes, R.N. Correia, Deposition of bioactive glass-ceramic thin-films by RF magnetron sputtering, J. Eur. Ceram. Soc. 23 (7) (2003) 1027–1030.
[29] G.E. Stan, C.O. Morosanu, D.A. Marcov, I. Parsuk, F. Miculescu, G. Reumont, Effect of Anealing Upon the Structure and Adhesion Properties of Sputtered Bio-Glass/Titanium Coatings, Appl. Surf. Sci. 255 (22) (2009) 9132–9138.
[30] B. Stuart, M. Gimeno-Fabra, J. Segal, I. Ahmed, D.M. Grant, Preferential sputtering in phosphate glass systems for the processing of bioactive coatings, Thin Solid Films (2015).
[31] B.W. Stuart, J.J. Titman, M. Gimeno-Fabra, I. Ahmed, D.M. Grant, Insights into structural characterisation and thermal properties of compositionally equivalent vapour-condensed and melt quenched glasses, Mater. Design (2016).
[32] P. Haque, I. Ahmed, A. Parsons, R. Felfel, G. Walker, C. Rudd, Degradation Properties and Microstructural Analysis of $40P_2O_5$—24MgO—16CaO—$16Na_2O$—$4Fe_2O_3$ Phosphate Glass Fibres, JNCS 375 (2013) 99–109.
[33] M.S. Hasan, I. Ahmed, A.J. Parson, G.S. Walker, C.A. Scotchford, Material characterisation and cytocompatibility assessment of quinternary phosphate glasses, J. Mater. Sci. Mater. Med. 23 (10) (2012) 2531–2541.
[34] I. Ahmed, A.J. Parson, C.D. Rudd, S.N. Nazhat, J.C. Knowles, P. Guerry, M.E. Smith, Comparison of phosphate-based glasses in the range $50P_2O_5$–(50–x)CaO–xNa_2O prepared using different precursors, Eur. J. Glass Sci. Technol. A 49 (2) (2007) 63–72.
[35] B.W. Stuart, M. Gimeno-Fabra, J. Segal, I. Ahmed, D.M. Grant, Degradation and characterization of resorbable phosphate-based glass thin-film coatings applied by radio-frequency magnetron sputtering, ACS Appl. Mater. Interfaces 7 (49) (2015) 27362–27372.
[36] M.E. Minitti, M.D. Lane, J.L. Bishop, A new hematite formation mechanism for Mars, Meteorit. Planet. Sci. 40 (1) (2005) 55–69.
[37] Y. Wang, A. Muramatsu, T. Sugimoto, FTIR analysis of well-defined α-Fe_2O_3 particles, Colloids Surf. Physicochem. Eng. Aspects 134 (3) (1998) 281–297.
[38] S. Zhang, L. Li, A. Kumar, Materials Characterization Techniques, Taylor & Francis Group, 2009.
[39] R.P. Gupta, S.K. Sen, Calculation of multiplet structure of core p-vacancy levels, PhRvB 10 (1) (1974) 71–77.
[40] A. Grosvenor, B. Kobe, N. McIntyre, Studies of the oxidation of iron by water vapour using X-ray photoelectron spectroscopy and QUASES™, Surf. Sci. Rep. 572 (2) (2017) 217–227.
[41] A. Grosvenor, B. Kobe, M. Biesinger, N. McIntyre, Investigation of multiplet splitting of Fe 2p XPS spectra and bonding in iron compounds, Surf. Interface Anal. 36 (12) (2004) 1564–1574.
[42] K.J. Rao, Structural Chemistry of Glasses, Elsevier, 2002.
[43] J.C. Knowles, Phosphate based glasses for biomedical applications, J. Mater. Chem. 13 (10) (2003) 2395–2401.
[44] J.R. Jones, Review of bioactive glass: from Hench to hybrids, Acta Biomater. 9 (1) (2013) 4457–4486.
[45] A. Boyd, M. Akay, B. Meenan, Influence of target surface degradation on the properties of rf magnetron-sputtered calcium phosphate coatings, Surf. Interface Anal. 35 (2) (2003) 188–198.
[46] A.R. Boyd, H. Duffy, R. McCann, B.J. Meenan, Sputter deposition of calcium phosphate/titanium dioxide hybrid thin films, MSEng C (28) (2008) 228–236.
[47] R.F. Cooper, J.B. Fanselow, D.B. Poker, The mechanism of oxidation of a basaltic glass: chemical diffusion of network-modifying cations, Geochim. Cosmochim. Acta 60 (17) (1996) 3253–3265.
[48] G.B. Cook, R.F. Cooper, Iron concentration and the physical processes of dynamic oxidation in an alkaline earth aluminosilicate glass, Am. Mineral. 85 (3–4) (2000) 397–406.
[49] W. Wisniewski, R. Harizanova, G. Volksch, C. Russel, Crystallisation of iron containing glass-ceramics and the transformation of hematite to magnetite, CrystEngComm 13 (12) (2011) 4025–4031.
[50] P. Kofstad, High-temperature oxidation of titanium, J. Less Common Met. 12 (6) (1967) 449–464.
[51] M.V. Diamanti, B. Del Curto, M. Pedeferri, Interference colors of thin oxide layers on titanium, Color Res. Appl. 33 (3) (2008) 221.
[52] S. Kumar, T.S. Narayanan, S.G.S. Raman, S. Seshadri, Thermal oxidation of Ti6Al4V alloy: microstructural and electrochemical characterization, Mater. Chem. Phys. 119 (1) (2010) 337–346.
[53] Y.D. Zhao, Y.T. Qian, W.C. Yu, Z.Y. Chen, Surface roughness of alumina films deposited by reactive r.f. sputtering, Thin Solid Films 286 (1–2) (1996) 45–48.
[54] J.A. Toque, M.K. Herliansyah, M. Hamdi, A. Ide-Ektessabi, I. Sopyan, Adhesion failure behavior of sputtered calcium phosphate thin film coatings evaluated using microscratch testing, J. Mech. Behav. Biomed. Mater. 3 (4) (2010) 324–330.
[55] K.L. Mittal, Adhesion Measurement of Films & Coatings: Volume 2. **2001**.
[56] T.J Callahan, J.B. Gantenberg, B.E. Sands, Calcium phosphate (Ca-P coating) draft guidance for preparation of food and drug administration (FDA) sumbissions for orthopaedic and dental endosseuous implants 1196, A. S., Ed. American Society for Testing and Materials: Philadelphia, **1994**.
[57] ISO, ISO 13779-2:2008: Implants for surgery – Hydroxyapatite – Part 2: Coatings of hydroxyapatite. **2008**.
[58] K. Cheng, C. Ren, W. Weng, P. Du, G. Shen, G. Han, S. Zhang, Bonding strength of fluoridated hydroxyapatite coatings: a comparative study on pull-out and scratch analysis, Thin Solid Films 517 (17) (2009) 5361–5364.
[59] S. Cozien-Cazuc, A. Parsons, G. Walker, I. Jones, C. Rudd, Effects of aqueous aging on the mechanical properties of P40Na20Ca16Mg24 phosphate glass fibres, JMatS 43 (14) (2008) 4834–4839.
[60] V.M. Sglavo, E. Mura, D. Milanese, J. Lousteau, Mechanical properties of phosphate glass optical fibers, Int. J. Appl. Glass Sci. 5 (1) (2014) 57–64.
[61] J.L. Ong, L.C. Lucas, W.R. Lacefield, E.D. Rigney, Structure, solubility and bond strength of thin calcium phosphate coatings produced by ion beam sputter deposition, Biomaterials 13 (4) (1992) 249–254.
[62] E. Stan, A.C. Popa, A.C. Galca, G. Aldica, J.M.F. Ferreira, Strong bonding between sputtered bioglass?ceramic films and Ti-substrate implants induced by atomic inter-diffusion post-deposition heat-treatments, Appl. Surf. Sci. 280 (2013) 530–538.
[63] G.E. Stan, A.C. Popescu, I.N. Mihailescu, D.A. Marcov, R.C. Mustata, L.E. Sima, S.M. Petrescu, A.R. Ianculescu, R. Trusca, C.O. Morosanu, On the bioactivity of adherent bioglass thin films synthesized by magnetron sputtering techniques, Thin Solid Films 518 (21) (2010) 5955–5964.
[64] C. Berbecaru, G.E. Stan, S. Pinac, D.U. Tulyaganov, J.M.F. Ferreira, The bioactivity mechanism of magnetron sputtered bioglass thin films, Appl. Surf. Sci. 258 (2012) 9840–9848.
[65] G.E. Stan, S. Pina, D.U. Tulyaganov, J.M. Ferreira, I. Pasuk, C.O. Morosanu, Biomineralization capability of adherent bio-glass films prepared by magnetron sputtering, J. Mater. Sci. Mater. Med. 21 (4) (2010) 1047–1055.
[66] G.E. Stan, D.A. Marcov, I. Pasuk, F. Miculescu, S. Pina, D.U. Tulyaganov, J.M.F. Ferreira, Bioactive glass thin films deposited by magnetron sputtering technique: the role of working pressure, Appl. Surf. Sci. 256 (23) (2010) 7102–7110.
[67] G.E. Stan, D. Bojin, Adherant glass-ceramic thin layer with bioactive potential deposited by magnetron sputtering techniques, U.P.B. Sci. Bull., Series B 72 (2) (2010) 187–196.
[68] J. Elmer, T. Palmer, S. Babu, E. Specht, In situ observations of lattice expansion and transformation rates of α and β phases in Ti–6Al–4V, Mater. Sci. Eng. A 391 (1) (2005) 104–113.
[69] B.C. Bunker, G.W. Arnold, J.A. Wilder, Phosphate glass dissolution in aqueous solution, J. Non-Cryst. Solids 64 (3) (1984) 291–316.
[70] H. Gao, T. Tan, D. Wang, Dissolution mechanism and release kinetics of phosphate controlled release glasses in aqueous medium, J. Control Release 96 (1) (2004) 29–36.
[71] J. Choueka, J.L. Charvet, H. Alexander, Y.H. Oh, G. Joseph, N.C. Blumenthal, W.C. LaCourse, Effect of annealing temperature on the degradation of reinforcing fibers for absorbable implants, J. Biomed. Mater. Res. 29 (11) (1995) 1309–1315.
[72] S. Cozien-Cazuc, A.J. Parsons, G.S. Walker, I.A. Jones, C.D. Rudd, Real-time dissolution of P40Na20Ca16Mg24 phosphate glass fibers, J. Non-Cryst. Solids 355 (50–51) (2009) 2514–2521.
[73] S. Maeno, Y. Niki, H. Matsumoto, H. Morioka, T. Yatabe, A. Funayama, Y. Toyama, T. Taguchi, J. Tanaka, The effect of calcium ion concentration on osteoblast viability, proliferation and differentiation in monolayer and 3D culture, Biomaterials 26 (23) (2005) 4847–4855.
[74] G.R. Beck, E. Moran, N. Knecht, Inorganic phosphate regulates multiple genes during osteoblast differentiation, including Nrf2, Exp. Cell Res. 288 (2) (2003) 288–300.
[75] L. He, X. Zhang, B. Liu, Y. Tian, W. Ma, Effect of magnesium ion on human osteoblast activity, Braz. J. Med. Biol. Res. 49 (7) (2016).
[76] T. Diamond, R. Pojer, D. Stiel, A. Alfrey, S. Posen, Does iron affect osteoblast function? Studies In vitro and in patients with chronic liver disease, Calcif. Tissue Int. 48 (6) (1991) 373–379.
[77] I. Sondi, B. Salopek-Sondi, Silver nanoparticles as antimicrobial agent: a case study on E. coli as a model for Gram-negative bacteria, J. Colloid Interface Sci. 275 (1) (2004) 177–182.